PNAS RESEARCH ARTICLE | CHEMISTRY

Metal–organic cycle-based multistage assemblies

Yan Sun[a,1], Wei Tuo[a], and Peter J. Stang[a,1]

Contributed by Peter J. Stang; received December 11, 2021; accepted February 11, 2022; reviewed by Marcetta Darensbourg and Vivian Yam

It is well known that chemical compositions and structural arrangements of materials have a great influence on their resultant properties. Diverse functional materials have been constructed by using either biomolecules (peptides, DNA, and RNA) in nature or artificially synthesized molecules (polymers and pillararenes). The relationships between traditional building blocks (such as peptides) have been widely investigated, for example how hydrogen bonds work in the peptide multistage assembly process. However, in contrast to traditional covalent bond-based building blocks-based assembly, suprastructures formed by noncovalent bonds are more influenced by specific bond features, but to date only a few results have been reported based on noncovalent bond-based building block multistage assembly. Here, three metal–organic cycles (MOCs) were used to show how coordination bonds influence the bimetallacycle conformation then lead to the topology differences of MOC multilevel ordered materials. It was found that the coordination linker (isophthalate-Pt-pyridine) is an important factor to tune the shape and size of the MOC-derived suprastructures.

metal–organic cycle (MOC) | multilevel ordering suprastructures (MOS) | multistage assembly

Significance

Different from polymers or peptides (lacking metals), metal–organic cycles (MOCs) have properties which arise from the combination of metals and common nonmetal elements and topologies. The development of MOC supramolecular materials is in its infancy, and how the coordination bonds work to make the corresponding suprastructures is unknown. This has limited the potential application of these MOC-based materials. Considering the applications of individual MOCs, the study and discovery of the unique factors in MOC-involved multilevel self-assembly are critical to further our knowledge of the underlying molecular mechanisms of metal-containing compounds. Here, a systematic study of MOC assembly in various solvent systems has confirmed the critical role of coordination linkers in tuning the shape and size of the MOC-derived suprastructures.

In nature, as a typical bottom-up method to create functional materials, self-assembly has been employed by all living organisms to provide important compounds to perform various biological functions. Inspired by nature, self-assembly has been used as a powerful tool to create artificial multifunctional materials with specific functions (1). In these dynamic systems, the as-obtained suprastructures emerge as products after countless self-corrections associated with the balance of weak interactions (2–5). In general, hydrogen bonds, aromatic stacking, metal coordination, hydrophobic/hydrophilic, and electrostatic interactions are involved in the assembly process. In the past, proteins (6), macromolecules (7, 8), and polymers (9) were used as building blocks to prepare nanofibers (10), nanovesicles (11), and networks (12). With the advance of the self-assembly method, multicomponent and multistage assembly have been developed for obtaining more complicated applications (13). As a result, these materials can be used to prepare semiconductors (14), smart devices (15), etc. As a consequence, the as-prepared material can be further used as electronic skin (16) to monitor dynamically pulsing cardiomyocytes (17).

Chemical components have a considerable influence on the resultant properties, and although a large number of suprastructures have been prepared from peptides and polymers, their properties have been restricted via the limited elements involved. Thus, the building blocks with and without metal show a dramatic difference in their material properties. Therefore, studying the relationship between metal–organic suprastructures (MOS) and the resultant multiscale well-organized materials is important and necessary for generating new materials with specific properties. However, different from the achievements in traditional building blocks-based functional materials (the first polymer was reported in 1907) (18), the knowledge of building blocks such as MOS-based (the first being reported in 1983) (19) on multilevel and multistage assembly is still in its initial stage.

As compared to a typical MOS, metal–organic cycles/cages (MOCs) (20–24) are discrete, well-defined molecular entities with various metal centers that can be used as noncovalent bond-based building blocks (NBBs) for fabricating functional suprastructures. Compared with the building blocks obtained by the traditional covalent bonds, noncovalent bond-based units, such as MOCs (25–27), exhibit attractive advantages in catalysis, fluorescent sensors, gas separation, and biomedical diagnosis and can serve as emissive materials and artificial biomolecular channels (28–38). For instance, MOCs exhibit a specific geometry depending on their precursor angle. To date, a series of MOCs with controllable geometries, including triangles (39), tetrahedra (40), rhomboids (41), hexagons (42), bimetallacycles (43), cuboctahedra (44), trigonal (45), and tetragonal prisms (46) have been prepared. Compared to their covalent bond-based building units, novel properties (47) appear due to their dynamic transformation features (48). For example, anthracene-based highly twisted metallacycles form instead of

Author affiliations: [a]Department of Chemistry, University of Utah, Salt Lake City, UT 84112

Author contributions: Y.S. and P.J.S. designed research; Y.S. performed research; Y.S. contributed new reagents/analytic tools; Y.S., W.T., and P.J.S. analyzed data; and Y.S., W.T., and P.J.S. wrote the paper.

Reviewers: M.D., Texas A&M University; and V.Y., University of Hong Kong.

The authors declare no competing interest.

[1]To whom correspondence may be addressed. Email: elaine.sun@utah.edu or stang@chem.utah.edu.

This article contains supporting information online at http://www.pnas.org/lookup/suppl/doi:10.1073/pnas.2122398119/-/DCSupplemental.

Published March 17, 2022.

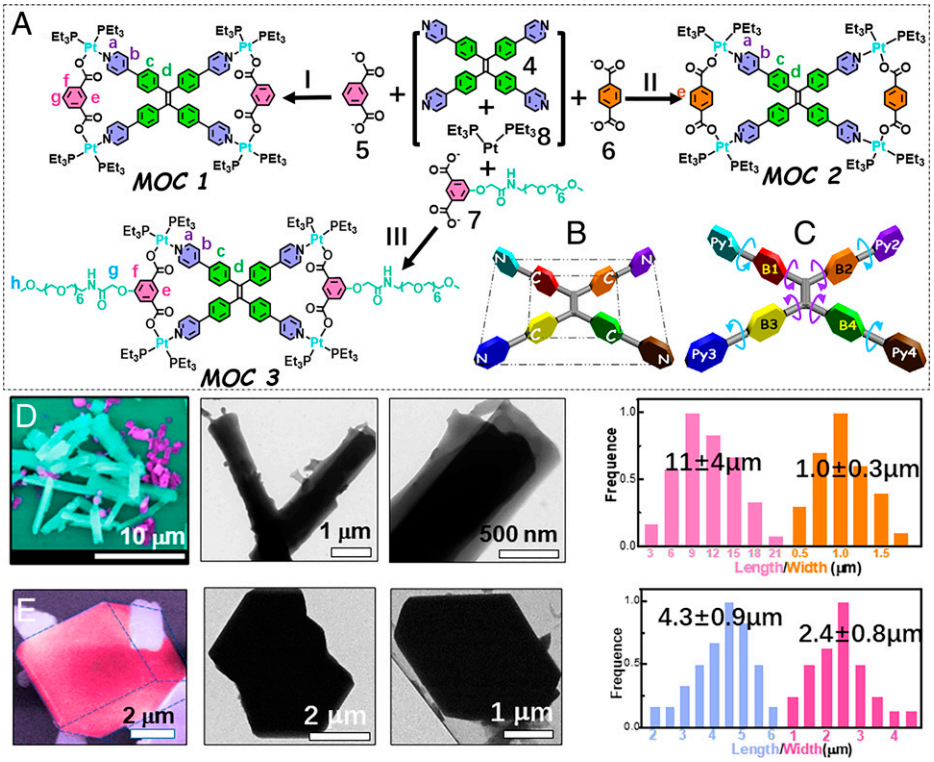

Scheme 1. (*A*) Synthesis of **MOCs 1–3** through coordination-driven assembly. (*B*) Cartoon showing the C–C, N–N, and Pt–Pt distances. (*C*) Dihedral angles between benzene rings and pyridine rings and other pyridine rings/dicarboxylate-related angles. SEM, TEM images (false color were used to label assemblies with different morphologies), and corresponding histograms of (*D*) **MOC 1**-based linear assemblies and (*E*) **MOC 2**-based nonlinear assemblies formed in DCM/TOL at DCM contents of 50% (10 μM).

the expected square formed by coordination-driven self-assembly (49). Tetra-(4-pyridylphenyl)-ethylene (TPPE)-based MOCs maintain the tetragonal prism geometry in $CHCl_3$ but exist as a bimetallacycle in dichloromethane (DCM). This solvent-templated synthesis of MOCs with various geometries is based on the incorporation of metallacrown recognition units into a flexible nanostructure, which allows the generation of solvent-specific binding pockets (50). Everything from their chemical/physical properties to their biomedical activities and catalysis was found to be influenced by their suprastructures (51, 52).

Compared with covalent bond building blocks, CBBs-related assembly, suprastructure construction involving NBBs is more complicated and requires more delicate control for balancing weak interactions (53). Specifically, how to tune the balance between NBBs and solvents and facilitate the self-assembly/correction of NBBs during the dynamic process is a challenge (54–56). Different from the mature methods for preparation and use of polymer-based materials (57), the first MOC-based multiscale ordering materials were only recently reported (15). On the other hand, the exact mechanism of suprastructure formation in these self-assembly processes is not well understood. Thus, it is necessary and helpful to develop a systematic understanding of the relationships among MOCs, the resultant suprastructures, and the corresponding properties.

Results and Discussion

Preparation and Characterization of MOCs 1–3. In this work, **MOCs 1–3** were prepared using **TPPE** (**4**), *m*-dicarboxylate (**5**)/*p*-dicarboxylate (**6**)/(oligo(ethylene glycol))OEG-modified dicarboxylate (**7**), and *cis*-$(PEt_3)_2Pt(OTf)_2$ (**8**) via the coordination-driven self-assembly at 50 °C for 1 h (Scheme 1*A*). ^{1}H-NMR (*SI Appendix*, Figs. S1–S3), ^{31}P-NMR (*SI Appendix*, Figs. S4–S6), and electrospray ionization time-of-flight mass spectrometry data (*SI Appendix*, Figs. S7–S9) confirm the formation of **MOCs 1–3**. Light yellow single crystals of these MOCs were obtained by slow diffusion in dichloromethane and ethyl acetate at 25 °C (*SI Appendix*, Table S1). It is shown that MOCs have differing space groups of triclinic P-1 (**MOC 1**), monoclinic c2/c (**MOC 2**), and triclinic P-1 (**MOC 3**) when the ligands change from *m*-dicarboxylate to *p*-dicarboxylate and then OEG-modified dicarboxylate. The atomic distances and dihedral angles change with the substituent employed (Scheme 1 *B* and *C*). Subsequently, **MOCs 1–3** were designed as a model system to study how the MOCs' structural difference influences the differences in morphology with changes in the ligand from *m*-dicarboxylate to *p*-dicarboxylate.

Characterization of the Resultant Suprastructures. The structural features of these three MOCs allow us to conclude with considerable confidence the characteristics that influence higher-level assembly. A DCM/toluene (TOL) solvent system of three different ratios was used to investigate further the assembly behaviors of **MOCs 1–3**. Optical microscopy, scanning electron microscopy (SEM), and transmission electron microscopy (TEM) were employed to characterize the resultant suprastructures.

At TOL 50%, assemblies obtained from **MOC 1** have linear suprastructures (Scheme 1*D* and *SI Appendix*, Fig. S10), and the **MOC 2**-based aggregates show nonlinear (cubic) suprastructures (Scheme 1*E* and *SI Appendix*, Fig. S11). Specifically, SEM and TEM images (Scheme 1*D*, *Left* and *Middle*) show the linear assemblies with lengths around 10 μm, and the enlarged image in Scheme 1*D* also shows these aggregates were stacked in layers. For **MOC 2**, instead of *m*-dicarboxylate, if *p*-dicarboxylate is used as a linker in bimetallacycle the resultant suprastructures change from linear to cubic morphology

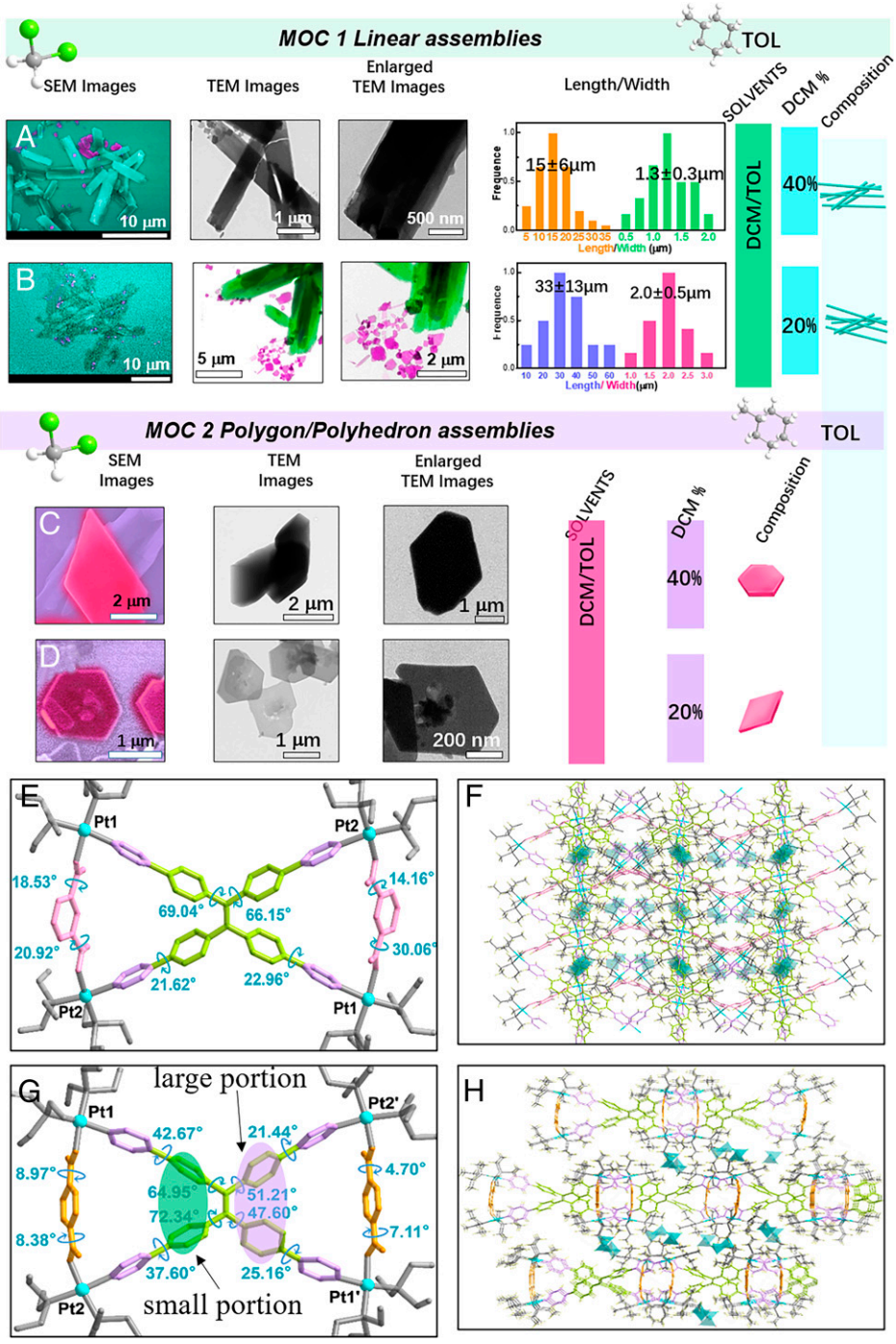

Fig. 1. SEM and TEM images (false color were used to label assemblies with different morphologies) and corresponding histograms of **MOC 1**-based linear assemblies (*A* and *B*) and **MOC 2**-based nonlinear assemblies (*C* and *D*) formed in DCM/TOL at DCM contents of (*A*) 40% and (*B*) 20% (10 μM). X-ray single-crystal structure of dihedral angles between benzene rings and pyridine rings and 3D structure along the a-axis of **MOC 1** (*E* and *F*) and **MOC 2** (*G* and *H*).

(Scheme 1*D*, *Left*). In particular, the rhomboid suprastructure (Scheme 1*E*, *Right*) indicates not only cubic suprastructures but also other polyhedra were formed when *p*-dicarboxylate was used as a ligand. Histograms show the linear aggregates with a length of 11 ± 4 μm and width of 1.0 ± 0.3 μm (Scheme 1*D*, *Right*). For polyhedra, the length is 4.3 ± 0.9 μm (Scheme 1*E*, *Right*). However, no aggregates were observed from **MOC 3** (using *m*-dicarboxylate, OEG-modified dicarboxylate as a linker) in the same solvent environment due to the better solubility of OEG.

It is found that the wire size increased from 15 ± 6 μm (length) and 1.3 ± 0.3 μm (width) to 33 ± 13 μm (length) and 2.0 ± 0.5 μm (width) as the TOL ratio increased from 60 to 80%. In particular, besides wires, small sheets (labeled purple) were also observed (Fig. 1 *A* and *B*). These results indicated that the morphological compositions and assembly purity of **MOC 1** were influenced by the TOL ratio (*SI Appendix*, Figs. S12 and S13). However, for **MOC 2**, increasing TOL ratio resulted in the morphology changes from polyhedron (50% TOL, Scheme 1*E*) to polygon (80% TOL). As shown in Fig. 1*C*, **MOC 2**-based rhomboid prisms (red) were obtained at a TOL ratio of 60%. A continuous increase in the TOL content promoted the formation of hexagonal sheets (Fig. 1*D* and *SI Appendix*, Figs. S14 and S15), indicating the

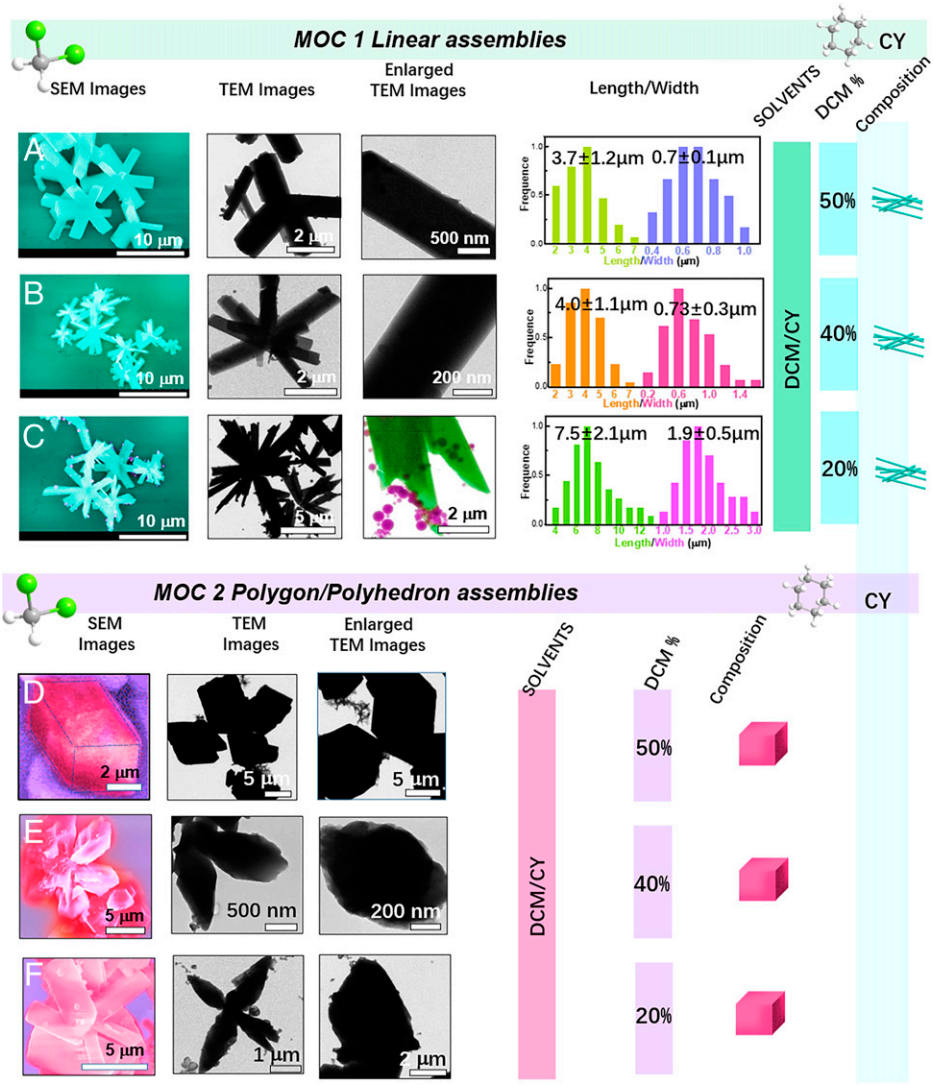

Fig. 2. SEM and TEM images (false color were used to label assemblies with different morphologies) and corresponding histograms of **MOC 1**-based linear assemblies (*A–C*) and **MOC 2**-based nonlinear assemblies (*D–F*) formed in DCM/CY at DCM contents of 50%, 40%, and 20% (10 μM).

TOL content can be used to tune the morphology while it cannot be used as a parameter to tune the size of the nonlinear aggregates.

The influence of the dicarboxylate linker on the resultant multilevel suprastructures was further confirmed by the second solvent system DCM/cyclohexane (CY). Fig. 2 *A–C* shows micrometer rods are the dominant morphology when using **MOC 1** for multistage assembly (*SI Appendix*, Fig. S17–S19), confirming the relationship between **MOC 1** and linear aggregates. Under the same experimental conditions, polygon and polyhedra were observed when using **MOC 2** for multistage assembly (Fig. 2 *D–F*), confirming the relationship between **MOC 2** and nonlinear aggregates. For **MOC 2**, just as with the DCM/TOL solvent system, a DCM/CY solvent system can be used to tune the size by changing the CY content from 50 to 80% (*SI Appendix*, Figs. S20–S22).

MOC conformation influence on multistage assembly was further confirmed by the third solvent system, DCM/dioxane (DX). As shown in *SI Appendix*, Figs. S23–S25, only linear suprastructures were formed by **MOC 1**, and no **MOC 2** hierarchical aggregates were observed. Specifically, in the DCM/DX system, the length of **MOC 1** wires decreased from 67 ± 17 μm to 28 ± 9 μm then to 20 ± 6 μm and the corresponding widths increased, when the DCM content increased from 20 to 40% then to 50%. Likewise, the fourth solvent system, DCM/ethyl acetate, brought about the formation of similar linear suprastructures for **MOC 1** (*SI Appendix*, Fig. S26), whereas only nonlinear aggregates were observed for **MOC 2** in the same solvent system.

Based on above results, the formation of **MOC 1**-based linear suprastructures is most likely to be structure-dependent rather than solvent-dependent, since similar linear morphologies have been observed in various solvent systems with a wide range of polarities and structural properties. To gain insight into the mechanism of structure-dependent morphogenesis, more information about the organization of metallacycles in three-dimensional (3D) suprastructures was provided by the stacking mode of MOCs crystals. After the formation of coordination bonds, **MOCs 1–3** have different symmetries in atomic distances and dihedral angles (*SI Appendix*, Fig. S16). Specifically, for **MOC 1**, the same atomic distances (C to C, N to N, Pt to Pt, and P to P) and dihedral angles (Fig. 1*E*) demonstrate the symmetry of the bimetallacycle at the structural level, resulting in the parallel stacking mode of **MOC 1** (Fig. 1*F*). As a result, linear aggregates can be observed in **MOC 1**-based multistage assembly (Fig. 1 *A* and *B*). For **MOC 2**, because of the difference in the dihedral angle twist after

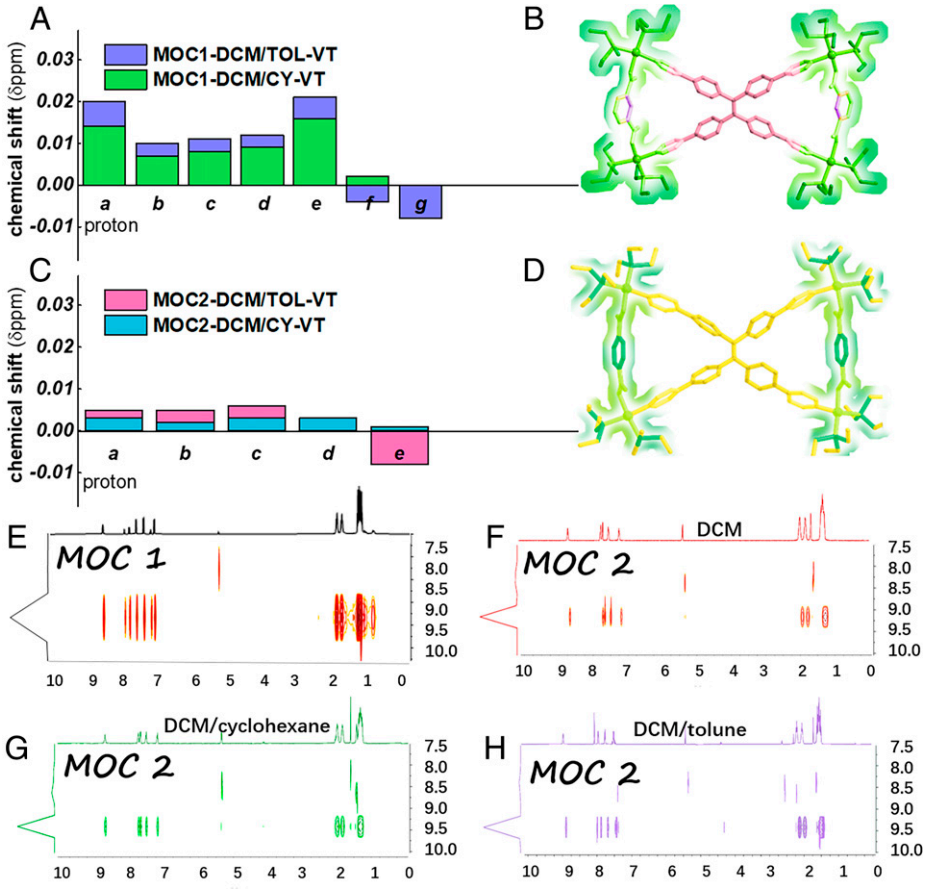

Fig. 3. Histograms show the changes in chemical shifts of (*A*) **MOC 1** and (*C*) **MOC 2** in DCM/CY (CD_2Cl_2/cyclohexane-d_{12} = 8:2, 100 μM) and DCM/TOL (CD_2Cl_2/toluene-d_8 = 8:2, 100 μM) at 15 to 30 °C; chemical shifts-based color span shows isophthalate-Pt-pyridine (green region, coordination bonds as linkage) are more flexible than TPE part in (*B*) **MOC 1** and (*D*) **MOC 2**. DOSY NMR spectra of **MOC 1** in DCM (*E*) and **MOC 2** in (*F*) DCM, (*G*) DCM/CY, and (*H*) DCM/TOL.

coordination bond formation, asymmetry can be easily observed. The green part of the model diagram represents the narrow portion of the molecule, and the purple part represents the wide portion of the molecule (Fig. 1*G*). The asymmetry of the two benzene rings on each side plays an important role in determining the stacking mode. To reduce steric hindrance, an alternating stacking mode is adopted (Fig. 1*H*). As a result, nonlinear aggregates were formed in this case (Fig. 1 *C* and *D*).

Variable-temperature NMR spectroscopy. Variable-temperature NMR (VT-NMR) was applied to gain further insight into the multistage assembly process, providing evidence that carboxylate ligands serve as important moieties to adjust the organization of bimetallacyles through their flexible features. As shown in Fig. 3, in both DCM/CY and DCM/TOL solvent systems **MOC 1** exhibited noticeable chemical shift changes (Fig. 3 *A* and *B*), whereas almost no changes were observed for **MOC 2** except that a slight upfield shift in the protons of *p*-dicarboxylate was detected after increasing temperature from 15 °C to 30 °C in DCM/TOL (Fig. 3 *C* and *D*). This phenomenon indicates that the electron cloud density increases and the shielding increases, since the benzene rings of *p*-dicarboxylate are turned outward. Specifically, the proton NMR spectra of **MOC 1** show smaller chemical shift changes in DCM/TOL than in DCM/CY (Fig. 3*A* and *SI Appendix*, Figs. S29 and S30), which indicates that **MOC 1** is more flexible in cyclohexane than in TOL. Such solvent-dependent flexibility of **MOC 1** could be attributed to the hydrophobic interactions between solvent molecules and MOCs, which influence the stacking mode of MOCs.

Crystal data (*SI Appendix*, Fig. S31) provided further information on the flexibility of **MOCs 1** and **2**. By comparing the weak interaction distributions in **MOCs 1** and **2**, it was shown that COO^--PEt_3, OTf-PEt_3, and OTf-Py existed in both **MOC 1** (*SI Appendix*, Fig. S31*A*) and **MOC 2** (*SI Appendix*, Fig. S31 *B–D*). In **MOC 2**, these three interactions still acted as the main influence, whereas more interactions, such as pyridine rings and COO^-, PEt_3 and benzene rings, and OTf and pyridine rings, were found. These results further indicate that the bimetallacycle **MOC 2** is more hindered in the assembly process than **MOC 1**. In addition, more H-bonds in **MOC 2** than **MOC 1** were observed at the intramolecular level as well (*SI Appendix*, Tables S2–S4), and more hindrances for **MOC 2** were also found at the intermolecular level. The association of these interlayer bonds strengthens the suprastructures, leading to the formation of a more stable staggered stacking system (*SI Appendix*, Figs. S31 *E* and *F*, S32, and S33).

DOSY and ROESY NMR studies. Diffusion ordered spectroscopy (DOSY) experiments were used to get further insight into the MOC involved suprastructure systems construction. In DCM, the proton signals of **MOC 1** are correlated with a diffusion coefficient (*D*) of ~4.64 × 10^{-10} m^2/s (Fig. 3*E* and *SI Appendix*, Fig. S34); for **MOC 2**, *D* is 6.90 × 10^{-10} m^2/s (Fig. 3*F* and *SI Appendix*, Fig. S35). For **MOC 1**, due to the formation of microscale assemblies, resulting in the linear aggregates of these assemblies, no reasonable DOSY data can be obtained. For **MOC 2**, the results of the DOSY experiments show that the proton signals are correlated with a *D* value of ~6.90 ×

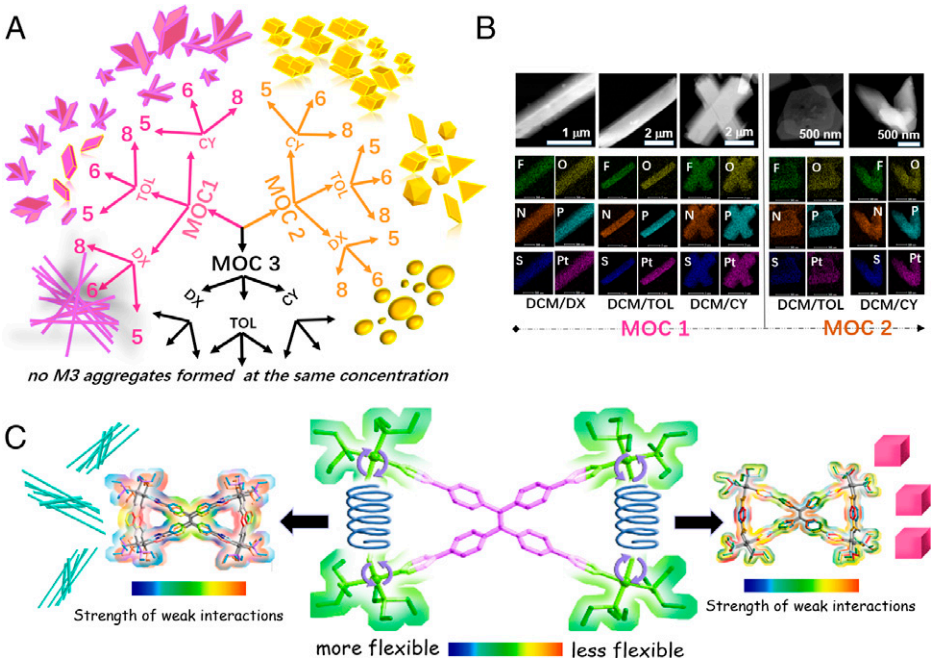

Fig. 4. (*A*) Scheme of **MOCs 1**- and **2**-based assemblies in DCM/DX, DCM/TOL, and DCM/CY. (*B*) STEM and EDS images of **MOCs 1**- and **2**-based assemblies. (*C*) Isophthalate-Pt-pyridine plays an essential regulatory role in multistage self-assembly.

10^{-10} m^2/s in DCM and decreased D of 3.80×10^{-10} m^2/s in DCM/TOL and 3.81×10^{-10} m^2/s in DCM/CY (Fig. 3 *F–H* and *SI Appendix*, Figs. S36 and S37), demonstrating the formation of larger aggregates in these solvent systems.

Rotating frame Overhauser enhancement spectroscopy (ROESY) NMR (*SI Appendix*, Figs. S38 and S39) was employed to study the influence of solvent systems and bimetallacycle structural features on the resultant molecular interactions. For both metallacycles (**MOC 1** and **MOC 2**) and the two solvent systems (DCM/CY and DCM/TOL), the long-range H–H coupling was observed between PEt_3 and H_a in pyridine (labeled scarlet in the insets of *SI Appendix*, Figs. S38 *C, D, F* and S39, named as PEt_3-Pt-Py region), which confirmed the formation of Pt–N coordination bonds. In addition, for the **MOC 1** DCM/TOL system, the long-range ^1H–^1H coupling is different from the rest of the systems and implies that the interactions among bimetallacycles change with the substituents/solvent systems through the hydrophobic interactions between MOCs and solvent molecules.

In addition to the similar interactions among TPPE moieties, ^1H–^1H coupling differences in DCM/TOL were observed, and thus solvent effects influence **MOC 1** multilevel assembly. Specifically, the scarlet region in **MOC 1** (*SI Appendix*, Fig. S38) coupling between H_{CH2}-/H_f instead of the previous couplings as found in DCM/CY, indicating there are interactions between methylene groups in the PEt_3 and the isophthalate. These observations provide more detail about how the solvent plays a special role in tuning the arrangement of MOCs through coordination bonds. For **MOC 2**, no such differences were observed in the two solvent systems (DCM/TOL and DCM/CY; *SI Appendix*, Figs. S38 *E* and *F* and S39). These outcomes are consistent with the observations during VT-NMR experiments. The different flexibility of **MOC 1** in the two solvent systems is probably due to the different stacking modes, which is in agreement with its different PEt_3– isophthalate interactions observed in ROESY spectra, whereas no significant flexibility differences were observed for **MOC 2** under the same experimental conditions, which is in line with its similar intramolecular interactions in the two solvent systems.

The cooperation of molecular structures and solvents in controlling the assembly was further confirmed by the chemical shift changes after the addition of CY or TOL (*SI Appendix*, Fig. S40). Generally, TOL was found to induce more significant chemical shifts than CY (*SI Appendix*, Figs. S41–S48).

Fig. 4 shows that the influence of MOCs' structural features and solvent system on the assembly extends from ligand-influenced coordination level forming the MOCs to a higher intra-MOC level that leads to variations in topology as well as size. As shown on the left side in Fig. 4*A*, one-dimensional linear assemblies can be formed by **MOC 1**. In particular, the length decreases as the solvent system changes from DCM/DX to DCM/TOL to DCM/CY. The right side shows nonlinear aggregates in yellow such as two-dimensional polygons and 3D polyhedrons that can be formed by **MOC 2**. Scanning TEM (STEM) and energy-dispersive X-ray spectroscopy (EDS) images of the typical elements (Pt, F, O, N, P, and S) show the uniform distribution of MOCs across the assemblies (Fig. 4*B*), whereas no aggregates are formed by **MOC 3** under the same conditions. Fig. 4*C* represents that isophthalate-Pt-pyridine (coordination bonds as linkage) plays an essential regulatory role in multistage self-assembly, which served as the most critical parameter for constructing supramolecular materials with various topological structures.

Conclusion

To date, various assemblies with complicated suprastructures have been obtained by different building blocks through self-assembly. With the advances in this field, more ligands with desired functions have been introduced to prepare building units, and a multistep assembly process was developed for more complex systems. However, in a system dominated by a series of weak interactions, how to best direct the coordination interactions, hydrogen bonds, and aromatic stacking is quite important. This work demonstrates how ligands influence the

coordination bond formation and determine the steric conformation of noncovalent building blocks, as well as how the hydrogen bond distributions in the building blocks influence the higher-level assembly by controlling the stacking mode. It was found that isophthalate-Pt-pyridine (coordination bonds via linkage) plays an essential regulatory role in multistage self-assembly, which served as the critical parameter for controlling the construction of supramolecular materials with various topological structures. As a result, MOC-derived suprastructures with controllable topologies, from linear wires/rods to nonlinear polygons/polyhedra, can be predicted and synthesized based on the cooperation of weak interactions. These findings pave the way to understand and control the suprastructure in multilevel assemblies by rationally designing coordination bond-based building blocks.

Materials and Methods

All reagents were commercially available and used as supplied without further purification. Deuterated solvents were purchased from Cambridge Isotope Laboratory. NMR experiments were recorded on a spectrometer at room temperature. ^{1}H NMR spectra were recorded in the designated solvents on a Varian Inova 400-MHz and a Bruker Neo 500-MHz spectrometers. $^{31}P\{^{1}H\}$ NMR spectra were recorded on a Varian Unity 300-MHz and a Bruker Neo 500-MHz spectrometers, and $^{31}P\{^{1}H\}$ NMR chemical shifts were referenced to an external unlocked sample of 85% H_3PO_4 (δ 0.0 ppm). Mass spectra were recorded on Waters TQD Acquity UPLC w/Acquity H Class UPLC mass spectrometer.

Data Availability. All study data are included in the article and/or *SI Appendix*.

ACKNOWLEDGMENTS. Y.S. and P.J.S. thank Ryan T. VanderLinden for single-crystal test work and H. Chen for mass spectra work.

1. G. Vantomme, E. W. Meijer, The construction of supramolecular systems. *Science* **363**, 1396–1397 (2019).
2. X. Yang *et al.*, Controlling O_2 reactivity in synthetic analogues of [NiFeS]- and [NiFeSe]-hydrogenase active sites. *J. Am. Chem. Soc.* **141**, 15338–15347 (2019).
3. R. Gu, J. M. Lehn, Constitutional dynamic selection at low reynolds number in a triple dynamic system: Covalent dynamic adaptation driven by double supramolecular self-assembly. *J. Am. Chem. Soc.* **143**, 14136–14146 (2021).
4. J. K. L. Poon, Z. Chen, S. Y. L. Leung, M. Y. Leung, V. W. W. Yam, Geometrical manipulation of complex supramolecular tessellations by hierarchical assembly of amphiphilic platinum(II) complexes. *Proc. Natl. Acad. Sci. U.S.A.* **118**, e2022829118 (2021).
5. T. Le, H. Nguyen, L. M. Perez, D. J. Darensbourg, M. Y. Darensbourg, Metal-templated, tight loop conformation of a Cys-X-Cys biomimetic assembles a dimanganese complex. *Angew. Chem. Int. Ed. Engl.* **59**, 3645–3649 (2020).
6. M. Yang, W. J. Song, Diverse protein assembly driven by metal and chelating amino acids with selectivity and tunability. *Nat. Commun.* **10**, s41467-019-13491-w (2019).
7. G. Yu *et al.*, A sugar-functionalized amphiphilic pillar[5]arene: Synthesis, self-assembly in water, and application in bacterial cell agglutination. *J. Am. Chem. Soc.* **135**, 10310–10313 (2013).
8. L. Li *et al.*, Resorcinarene induced assembly of carotene and lutein into hierarchical superstructures. *J. Am. Chem. Soc.* **142**, 20583–20587 (2020).
9. Y. Sun, W. Fu, Z. Li, Z. Wang, Tailorable aqueous dispersion of single-walled carbon nanotubes using tetrachloroperylene-based bolaamphiphiles via noncovalent modification. *Langmuir* **30**, 8615–8620 (2014).
10. Y. Sun *et al.*, Fine-tuned nanostructures assembled from L-lysine-functionalized perylene bisimides. *Langmuir* **27**, 11364–11371 (2011).
11. Y. Sun, W. Fu, C. Chen, J. Wang, Y. Yao, Water-soluble pillar[5]arene induced the morphology transformation of self-assembled nanostructures and had further application in paraquat detection. *Chem. Commun. (Camb.)* **53**, 3725–3728 (2017).
12. Y. Sun, J. Wang, Y. Yao, The first water-soluble pillar[5]arene dimer: Synthesis and construction of a reversible fluorescent supramolecular polymer network in water. *Chem. Commun. (Camb.)* **53**, 165–167 (2016).
13. Z. Álvarez *et al.*, Bioactive scaffolds with enhanced supramolecular motion promote recovery from spinal cord injury. *Science* **374**, 848–856 (2021).
14. H. Chen, J. F. Stoddart, From molecular to supramolecular electronics. *Nat. Rev. Mater.* **6**, 804–828 (2021).
15. Y. Sun *et al.*, Self-assembly of metallacages into centimeter films with tunable size and emissions. *J. Am. Chem. Soc.* **142**, 17933–17937 (2020).
16. A. Miyamoto *et al.*, Inflammation-free, gas-permeable, lightweight, stretchable on-skin electronics with nanomeshes. *Nat. Nanotechnol.* **12**, 907–913 (2017).
17. S. Lee *et al.*, Ultrasoft electronics to monitor dynamically pulsing cardiomyocytes. *Nat. Nanotechnol.* **14**, 156–160 (2019).
18. American Chemical Society, The Bakelizer. https://www.acs.org/content/acs/en/education/whatischemistry/landmarks/bakelite.html. Accessed 3 February 2022.
19. P. Stricklen, J. Verkade, Novel homo and heterometallic coordination macrocycles. *J. Am. Chem. Soc.* **105**, 2494–2495 (1983).
20. Y. Sun, C. Chen, J. Liu, P. J. Stang, Recent developments in the construction and applications of platinum-based metallacycles and metallacages via coordination. *Chem. Soc. Rev.* **49**, 3889–3919 (2020).
21. R. Chakrabarty, P. S. Mukherjee, P. J. Stang, Supramolecular coordination: Self-assembly of finite two- and three-dimensional ensembles. *Chem. Rev.* **111**, 6810–6918 (2011).
22. D. A. Roberts, B. S. Pilgrim, J. R. Nitschke, Covalent post-assembly modification in metallosupramolecular chemistry. *Chem. Soc. Rev.* **47**, 626–644 (2018).
23. A. M. Lifschitz, M. S. Rosen, C. M. McGuirk, C. A. Mirkin, Allosteric supramolecular coordination constructs. *J. Am. Chem. Soc.* **137**, 7252–7261 (2015).
24. D. L. Caulder, K. N. Raymond, Supermolecules by design. *Acc. Chem. Res.* **32**, 975–982 (1999).
25. J. Singh *et al.*, The first quantitative synthesis of a closed three-link chain (6_1^3) using coordination and noncovalent interactions-driven self-assembly. *J. Am. Chem. Soc.* **142**, 9327–9336 (2020).
26. A. J. Gosselin, C. A. Rowland, E. D. Bloch, Permanently microporous metal-organic polyhedra. *Chem. Rev.* **120**, 8987–9014 (2020).
27. T. R. Cook, Y. R. Zheng, P. J. Stang, Metal-organic frameworks and self-assembled supramolecular coordination complexes: Comparing and contrasting the design, synthesis, and functionality of metal-organic materials. *Chem. Rev.* **113**, 734–777 (2013).
28. H. Takezawa, K. Shitozawa, M. Fujita, Enhanced reactivity of twisted amides inside a molecular cage. *Nat. Chem.* **12**, 574–578 (2020).
29. A. S. Y. Law, L. C. C. Lee, K. K. W. Lo, V. W. W. Yam, Aggregation and supramolecular self-assembly of low-energy red luminescent Alkynylplatinum(II) complexes for RNA detection, nucleolus imaging, and RNA synthesis inhibitor screening. *J. Am. Chem. Soc.* **143**, 5396–5405 (2021).
30. C. Guo, A. C. Sedgwick, T. Hirao, J. L. Sessler, Supramolecular fluorescent sensors: An historical overview and update. *Coord. Chem. Rev.* **427**, 213560 (2021).
31. Y. Li *et al.*, Artificial biomolecular channels: Enantioselective transmembrane transport of amino acids mediated by homochiral zirconium metal-organic cages. *J. Am. Chem. Soc.* **143**, 20939–20951 (2021).
32. L. Z. Qin *et al.*, A series of functionalized zirconium metal-organic cages for efficient CO_2/N_2 separation. *Inorg. Chem.* **60**, 17440–17444 (2021).
33. X. Yan, T. R. Cook, P. Wang, F. Huang, P. J. Stang, Highly emissive platinum(II) metallacages. *Nat. Chem.* **7**, 342–348 (2015).
34. Y. Sun, C. Chen, F. Zhang, S. Jiang, P. J. Stang, Pt Metallacage-based centimeter films for smart emissive poly(N-isopropylacrylamide) hydrogel devices. *Mater. Chem. Phys.* **277**, 125544 (2022).
35. K. Acharyya *et al.*, Emissive Platinum(II) macrocycles as tunable cascade energy transfer scaffolds. *Angew. Chem. Int. Ed. Engl.*, 10.1002/anie.202200715 (2022).
36. K. Ghosh *et al.*, Coordination-driven self-assembly of cavity-cored multiple crown ether derivatives and poly[2]pseudorotaxanes. *J. Am. Chem. Soc.* **130**, 5320–5334 (2008).
37. X. Jiang *et al.*, From mechanically interlocked structures to host-guest chemist based on twisted dimeric architectures by adjusting space constraints. *CCS Chem.* **3**, 2042–2054 (2021).
38. P. C. Purba, M. Maity, S. Bhattacharyya, P. S. Mukherjee, A self-assembled Palladium(II) barrel for binding of fullerenes and photosensitization ability of the fullerene-encapsulated barrel. *Angew. Chem. Int. Ed. Engl.* **60**, 14109–14116 (2021).
39. H. Zhu *et al.*, Formation of planar chiral platinum triangles via Pillar[5]arene for circularly polarized luminescence. *J. Am. Chem. Soc.* **142**, 17340–17345 (2020).
40. Y. R. Zheng, W. J. Lan, M. Wang, T. R. Cook, P. J. Stang, Designed post-self-assembly structural and functional modifications of a truncated tetrahedron. *J. Am. Chem. Soc.* **133**, 17045–17055 (2011).
41. M. Zhang *et al.*, Metallacycle-cored supramolecular assemblies with tunable fluorescence including white-light emission. *Proc. Natl. Acad. Sci. U.S.A.* **114**, 3044–3049 (2017).
42. W. Tuo *et al.*, Pillar[5]arene-containing metallacycles and host-guest interaction caused aggregation-induced emission enhancement platforms. *J. Am. Chem. Soc.* **142**, 16930–16934 (2020).
43. Z. Yang *et al.*, Hierarchical self-assembly of a pyrene-based discrete Organoplatinum(II) double-metallacycle with triflate anions via hydrogen bonding and its tunable fluorescence emission. *J. Am. Chem. Soc.* **142**, 13689–13694 (2020).
44. K. Ghosh, J. Hu, H. S. White, P. J. Stang, Construction of multifunctional cuboctahedra via coordination-driven self-assembly. *J. Am. Chem. Soc.* **131**, 6695–6697 (2009).
45. X. Chang *et al.*, Self-assembled perylene bisimide-cored trigonal prism as an electron-deficient host for C_{60} and C_{70} driven by "Like Dissolves Like". *J. Am. Chem. Soc.* **142**, 15950–15960 (2020).
46. Y. Sun *et al.*, Self-assembly of metallacages into multidimensional suprastructures with tunable emissions. *J. Am. Chem. Soc.* **140**, 12819–12828 (2018).
47. H. Sepehrpour, W. Fu, Y. Sun, P. J. Stang, Biomedically relevant self-assembled metallacycles and metallacages. *J. Am. Chem. Soc.* **141**, 14005–14020 (2019).
48. S. Pullen, J. Tessarolo, G. H. Clever, Increasing structural and functional complexity in self-assembled coordination cages. *Chem. Sci. (Camb.)* **12**, 7269–7293 (2021).
49. C. Chen *et al.*, Formation of highly twisted metallacycle results in the emergence of anthracene based AIE effect. *Proc. Natl. Acad. Sci. U.S.A.* **118**, e2102602118 (2021).
50. B. Kilbas, S. Mirtschin, R. Scopelliti, K. Severin, A solvent-responsive coordination cage. *Chem. Sci. (Camb.)* **3**, 701–704 (2012).
51. Y. Sun, P. J. Stang, Metallacycles, metallacages and their aggregate/optical behavior. *Aggregate* **2**, e94 (2021).
52. Y. Xu *et al.*, Design of a metallacycle-based supramolecular photosensitizer for in vivo image-guided photodynamic inactivation of bacteria. *Angew. Chem. Int. Ed.*, 10.1002/anie.202110048 (2021).
53. R. Montis *et al.*, Complex structures arising from the self-assembly of a simple organic salt. *Nature* **590**, 275–278 (2021).
54. Y. Sun, C. Chen, P. J. Stang, Soft materials with diverse suprastructures via the self-assembly of metal-organic complexes. *Acc. Chem. Res.* **52**, 802–817 (2019).
55. D. N. Yan *et al.*, Photooxidase mimicking with adaptive coordination molecular capsules. *J. Am. Chem. Soc.* **143**, 16087–16094 (2021).
56. K. Carter-Fenk, K. U. Lao, J. M. Herbert, Predicting and understanding non-covalent interactions using novel forms of symmetry-adapted perturbation theory. *Acc. Chem. Res.* **54**, 3679–3690 (2021).
57. X. Shi *et al.*, Large-area display textiles integrated with functional systems. *Nature* **591**, 240–245 (2021).